Linear instability of the path of a freely rising spheroidal bubble

Joël Tchoufag, Jacques Magnaudet, David Fabre

Linear instability of the path of a freely rising spheroidal bubble

Joël Tchoufag[1], Jacques Magnaudet[1,2,†] and David Fabre[1]

[1]Université de Toulouse, INPT, UPS, IMFT (Institut de Mécanique des Fluides de Toulouse), Allée Camille Soula, F-31400 Toulouse, France

[2]CNRS, IMFT, F-31400 Toulouse, France

Path and wake instabilities of buoyancy-driven oblate spheroidal bubbles with a prescribed shape rising freely in a viscous fluid otherwise at rest are studied using global stability analysis, following the technique recently developed for a coupled fluid + body system by Tchoufag, Fabre & Magnaudet (*J. Fluid Mech.* vol. 740, 2014, pp. 278–311). The essential role of the wake on the path instability is evidenced by comparing the shape of the global stability diagram with that obtained in the case of a fixed bubble. However, dramatic differences are also found, since the critical curve of the coupled system mostly involves low- and high-frequency oscillating modes, whereas that of a fixed bubble only involves stationary modes. Comparison of the present predictions with results obtained through direct numerical simulation is achieved in several regimes, confirming the predictions of the linear approach but also highlighting some of its limitations when the system successively encounters several unstable modes.

Key words: drops and bubbles, instability, wakes/jets

1. Introduction

Path instability of isolated rising bubbles has been a subject of curiosity for ages, as testified by Leonardo's drawings (Prosperetti *et al.* ; Prosperetti). Various hypotheses on the origin of this puzzling behaviour were suggested during the second half of the last century (see the review by Magnaudet & Eames), including the effects of surfactants and the influence of shape oscillations. The picture was significantly clarified by the direct numerical simulations (DNS) of Mougin & Magnaudet ( ) and Magnaudet & Mougin ( ) with freely rising and fixed bubbles, respectively, which showed that path instability is closely related to wake instability. Both studies considered perfectly clean bubbles (i.e. the outer fluid obeyed a shear-free condition at the bubble surface) with a frozen oblate shape and revealed

† Email address for correspondence: magnau@imft.fr

that the wake becomes unstable when the oblateness exceeds some critical threshold, the value of which depends on the Reynolds number based on the rising speed.

Independently, recent theoretical and computational studies devoted to two- and three-dimensional freely rising/falling rigid bodies such as plates (Assemat, Fabre & Magnaudet), infinitely thin disks (Auguste, Magnaudet & Fabre ; Chrust, Bouchet & Dusek) or disks of finite thickness (Chrust, Bouchet & Dusek ; Tchoufag, Fabre & Magnaudet) have revealed that the translational and rotational body degrees of freedom generally play a key role in the path instability mechanism. In particular, they can cause the thresholds and frequencies of the observed paths to differ drastically from those associated with the wake instability of the fixed body. This is why assessment of the possible relation and differences between the primary destabilization of the wake and path of a freely moving bubble and the wake instability of a fixed bubble experiencing a uniform upstream flow is in order. As discussed by Tchoufag *et al.* (), this goal is best achieved by considering a global linear stability analysis (LSA) of the coupled fluid + body system. This is the approach followed here, the outline of which is given in § 2 before the main results are discussed in § 3. This section also provides some quantitative comparisons with the DNS results of Mougin & Magnaudet () (hereafter referred to as MM02) in various regimes.

2. Parameterization and formulation of the global stability problem

Following MM02, we assume the bubble to be a non-deformable spheroid characterized by the aspect ratio $\chi = b/a$ between the major and minor semiaxes. As shown in several experiments, e.g. Ellingsen & Risso (), this assumption is approximately valid as far as surface tension effects are of the same order as inertial effects. The problem also depends on the bubble-to-fluid density ratio $\overline{\rho}$, and on the Reynolds number $Re = U_0 d/\nu$, where $d = 2(b^2 a)^{1/3}$ is the bubble equivalent diameter, U_0 is the equilibrium velocity of its steady vertical rise (or base state) and ν is the fluid kinematic viscosity. Nevertheless, comparisons with experiments and DNS are made easier by replacing U_0 by the gravitational velocity $U_g = ((1-\overline{\rho})gd)^{1/2}$, which yields the Archimedes number $Ar = U_g d/\nu$, where g denotes gravity. The conversion from Re to Ar is achieved by determining the drag coefficient $C_D(Re)$ in the base state and equating the drag and buoyancy forces, which yields the relation $C_D(Re)Re^2 = 4Ar^2/3$. As is well known, Re and χ are not independent in real gas–liquid systems. Rather, given the fluid physical properties and bubble volume, they are uniquely determined by the Archimedes number and the Bond number $Bo = \rho(1-\overline{\rho})gd^2/\sigma$, where σ and ρ stand for the surface tension and liquid density, respectively. Hence, arbitrary variation of Re at a given χ or vice versa as we do here could only be achieved by independent variation of ρ, ν and σ in a laboratory experiment, which is generally not feasible.

Similarly to the formulation employed by Tchoufag *et al.* (), we introduce a system of axes (x, y, z) translating and rotating with the bubble, with x aligned with the spheroid axis and y and z lying in its diametrical plane. The bubble orientation is defined by the vector $\boldsymbol{\Xi}$ whose components are the roll/pitch/yaw angles corresponding respectively to the angular positions of the $x/y/z$ axes with respect to a fixed system of axes (x_0, y_0, z_0). The Navier–Stokes equations for the absolute velocity $\boldsymbol{V}$ and pressure P are written in the (x, y, z) reference frame; $\boldsymbol{V}$ falls to zero far from the bubble and obeys the zero-penetration condition $\boldsymbol{V}\cdot\boldsymbol{n} = 0$ and the shear-free condition $\boldsymbol{n}\times(\boldsymbol{T}\cdot\boldsymbol{n}) = \boldsymbol{0}$ at the bubble surface, where $\boldsymbol{n}$ denotes

the unit normal to this surface and $\boldsymbol{T} = -P\boldsymbol{I} + \nu(\boldsymbol{\nabla V} + {}^t\boldsymbol{\nabla V})$ is the stress tensor ($\boldsymbol{I}$ is the Kronecker tensor). The Newton equations expressing the overall force and torque balances on the bubble govern the evolution of its translational velocity $\boldsymbol{U}$ and rotation rate $\boldsymbol{\Omega}$. Finally, for small deviations from vertical, the evolution of the bubble orientation is governed by the equation $\mathrm{d}\boldsymbol{\Xi}/\mathrm{d}t = \boldsymbol{\Omega}$.

The corresponding LSA problem is solved thanks to the finite element solver FreeFem++ already used by Tchoufag *et al.* ( ) for freely moving disks and by Tchoufag, Magnaudet & Fabre ( ) for fixed oblate bubbles. The reader is referred to these two references, especially the first one, for all technical details. As shown in Tchoufag *et al.* ( ), dealing with the shear-free condition in the framework of a variational formulation requires the normal stress, $\Sigma = \boldsymbol{n}\cdot\boldsymbol{T}\cdot\boldsymbol{n}$, to be considered as an additional unknown. The formulation described in Tchoufag *et al.* ( ) is modified accordingly and the vector state corresponding to the fluid unknowns is $\boldsymbol{Q}^f = [\boldsymbol{V}, P, \Sigma]$, where all variables depend on space and time. The complete state vector for the bubble + fluid system is then $\boldsymbol{Q} = [\boldsymbol{Q}^f, \boldsymbol{Q}^b]$, where $\boldsymbol{Q}^b = [\boldsymbol{U}, \boldsymbol{\Omega}, \boldsymbol{\Xi}]$ gathers the time-dependent bubble kinematic degrees of freedom.

In order to perform the global stability analysis, the state vector is split into a base state $\boldsymbol{Q}_0$ and a linear perturbation $\boldsymbol{q}$. The base state corresponds to the steady vertical rise of the bubble with zero inclination, i.e. the axis of the oblate spheroid is aligned with gravity, and is computed on a triangular grid (the influence of the grid characteristics is discussed by Tchoufag *et al.*) via a Newton algorithm (Sipp & Lebedev). By introducing the cylindrical coordinate system (r, ϕ, x) such that $y = r\cos\phi$, $z = r\sin\phi$, the perturbation is expanded in normal mode form as $\boldsymbol{q} = [\hat{\boldsymbol{q}}^f(r,x)\mathrm{e}^{\mathrm{i}m\varphi}, \hat{\boldsymbol{q}}^b]\mathrm{e}^{\lambda t}$. By linearizing the governing equations around the base state, the whole problem reduces to a generalized eigenproblem of the form $\mathscr{A}_m\hat{\boldsymbol{q}} = \lambda\mathscr{B}_m\hat{\boldsymbol{q}}$ (with $\hat{\boldsymbol{q}} = [\hat{\boldsymbol{q}}^f, \hat{\boldsymbol{q}}^b]$) for each value of the azimuthal wavenumber m. Finally, by making use of the SLEPc library, the eigenvalues $\lambda = \lambda_r + \mathrm{i}\lambda_i$ and the associated global modes $\hat{\boldsymbol{q}}$ are obtained for various sets of the control parameters χ and Re, the bubble-to-fluid density ratio being set to $\overline{\rho} = 10^{-3}$, which is typical of the air–water system under standard conditions. The results discussed below have been made dimensionless by normalizing lengths with d, velocities with U_0, time with d/U_0 and gravity with U_0^2/d.

3. Results and discussion

3.1. *Growth rates and frequencies as a function of Re and χ*

The most unstable modes all correspond to $|m| = 1$, as expected from the various available studies with axisymmetric bodies, i.e. fixed spheres and disks (Natarajan & Acrivos), fixed bubbles (Tchoufag *et al.*) or freely moving disks (Tchoufag *et al.*). These modes, with growth rate λ_r and reduced frequency $St = \lambda_i/(2\pi)$, have been computed over the range $\chi \in [2.1, 2.5]$ and $Re \lesssim 3\times10^3$. The upper value of χ was chosen after an attempt with $\chi = 2.7$ showed that it was difficult to accurately determine the near-zero growth rate at the highest values of Re involved ($\approx 5\times10^3$ in that case), due to difficulties in properly capturing the structure of the very thin boundary layer.

The curves $\lambda_r(Re)$ and $St(Re)$ obtained by continuously tracking the most significant eigenvalues as a function of Re for various values of χ are gathered in figure (*a–b*) and (*c–d*), respectively. The growth rate curves evidence a destabilization–restabilization behaviour of the system, with λ_r reaching a maximum at a value of Re that slightly increases with χ and ranges from 400 to 550 in the range of χ explored. Therefore, contrary to the case of buoyancy-driven rigid

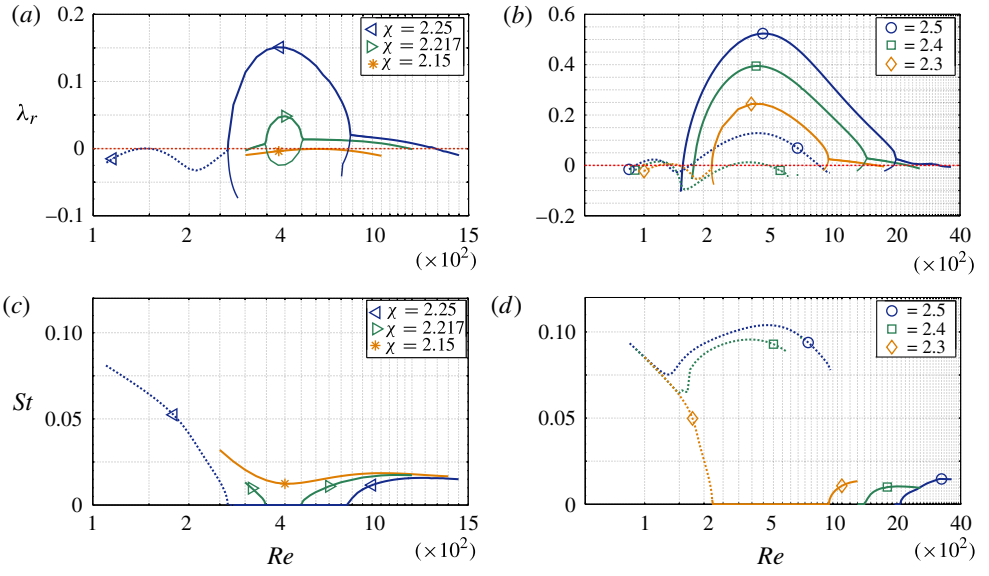

FIGURE 1. Variations of the growth rate (*a*,*b*) and reduced frequency (*c*,*d*) as a function of Re for several bubble aspect ratios: (*a*) and (*c*) $\chi = 2.15$–2.25; (*b*) and (*d*) $\chi = 2.3$–2.5. The dashed lines are associated with modes oscillating at a high quasi-constant frequency (*HF* modes); the thick solid lines correspond to stationary (*S*) or low-frequency (*LF*) modes or to combinations of both. The thin solid lines in (*a*) and (*b*) represent a second type of steady mode which at some point merges with the main *S* mode and gives birth to an *LF* mode, or sometimes (for $\chi = 2.25 - 2.3$ and $200 < Re < 300$) to an *HF* mode.

bodies, the path of a spheroidal bubble is unstable only within a finite range of Re whose span increases with χ. The fact that the vorticity resulting from the shear-free condition reaches a finite value when Re goes to infinity instead of increasing as $Re^{1/2}$ when the fluid obeys a no-slip condition is at the root of this specific behaviour, as discussed in detail by Magnaudet & Mougin ( ). Figure (*a*) indicates that the growth rate becomes negative whatever the value of Re for $\chi \leqslant \chi_C \approx 2.15$, a critical oblateness slightly less than the aspect ratio $\chi_W \approx 2.21$ corresponding to the threshold of wake instability in the fixed-bubble configuration (Magnaudet & Mougin ; Tchoufag *et al.*).

Analysis of the reduced frequencies in figure (*c*–*d*) allows us to identify three main kinds of unstable modes.

(i) First, the most prominent feature is the existence of an '*S*' family corresponding to stationary modes which are found to be unstable as soon as $\chi \gtrsim 2.215$. These modes have the largest range of existence for most values of χ; their amplification rate reaches a maximum in the range $400 \leqslant Re \leqslant 600$.

(ii) Second, we can identify an '*HF*' family of modes oscillating at a quasi-constant high frequency around the typical value $St \sim 0.1$ (dashed lines). For $\chi \lesssim 2.55$, these modes are unstable in two distinct intervals, the first one being located around $Re \approx 100$ and the second being centred at approximately $Re \approx 400$. For $\chi \gtrsim 2.55$ (not shown), these two intervals merge into a single one. It should be noted that for $\chi > 2.25$, these modes are the first that become unstable as the Reynolds number increases. This is strikingly different from the picture observed in the fixed-bubble configuration,

where the first bifurcation is always stationary (Magnaudet & Mougin ; Tchoufag *et al.*). Figure (*a*,*b*) shows that the *HF* modes always restabilize at high *Re*.

(iii) Third, we observe an '*LF*' family of modes oscillating at a quasi-constant but very low frequency, $St \sim 0.01$. These modes are mostly encountered in a range of Reynolds number located just above that corresponding to the existence of the *S* modes, and their amplification rate is in most cases much smaller than that of the *S* and *HF* modes. It should be noted that, compared with the *S* modes, their range of existence also extends to lower values of χ (see e.g. the case $\chi = 2.15$ in figure (*a*).

A closer look at the results shows that, in addition to the aforementioned three main families, a second subdominant stationary mode (thin lines in figure (*a*,*b*) is also present for $\chi \geqslant 2.25$ in a narrow interval of *Re* just below the upper threshold Re_f of the *S* mode. This mode helps in understanding the onset of the *LF* mode, which can be interpreted as a result of the merging of two real eigenvalues into a pair of complex conjugate eigenvalues (see e.g. the curve corresponding to $\chi = 2.4$). A similar process occurs close to the lower threshold of the *S* mode for $\chi \leqslant 2.3$, albeit in a much narrower range of χ (see e.g. the case $\chi = 2.217$ in figure (*a*). A more detailed view which allows one to fully appreciate how this merging/splitting process occurs is provided in appendix A where the unstable eigenvalue corresponding to $\chi = 2.217$ is tracked in the complex plane.

Combination of the information contained in figure (*a*,*b*) reveals that all curves involving a stationary mode in some range of *Re* are actually made of a succession of the above families of modes. Hence, for a given aspect ratio, sudden frequency variations or 'jumps' are observed when the system switches from one mode to another. For instance, as *Re* increases, *St* goes from 0.1 to 0 and then to 0.01, corresponding to an *HF*–*S*–*LF* sequence at $\chi = 2.3$, or from approximately 0.01 to 0 and then to 0.01 again for the *LF*–*S*–*LF* sequence at $\chi = 2.217$. As we shall show below, these frequency changes are associated with dramatic changes in the spatial structure of the corresponding global modes.

3.2. *Stability diagrams*

By tracking the *Re* values such that $\lambda_r(Re) = 0$ and the corresponding frequencies, we obtain the phase diagrams in the planes (χ, *Re*) and (χ, *St*) as drawn in figure . It is immediately seen that the *HF*, *LF* and *S* modes are unstable only for aspect ratios larger than the threshold values $\chi_{C_{HF}} \simeq 2.25$, $\chi_{C_{LF}} \simeq 2.15$ and $\chi_S \simeq 2.215$, respectively. Hence, path instability of spheroidal bubbles with a frozen shape is found to exist only for $\chi \geqslant \chi_C = 2.15$.

The grey lines in figure (*a*) correspond to the neutral stability curves of the wake alone, as obtained by Tchoufag *et al.* ( ) for a fixed spheroidal bubble. Comparison of these curves with those of the fluid + bubble system reveals that the destabilization or restabilization thresholds of the wake are quite close to those of the coupled system, underlining the central role of the wake in the path instability mechanism. However, crucial differences may be noticed. First, the primary instability as *Re* increases is found to be of *HF* type for $\chi > 2.25$, at odds with the fixed-bubble analysis which predicts the first bifurcation to be stationary for all $\chi \geqslant 2.21$. Second, instability is found to occur in the form of an *LF* mode for $2.15 \leqslant \chi \leqslant 2.215$, a range where the wake of a fixed bubble is stable whatever the value of *Re*. Hence, it is only within the narrow range $\chi \in [2.215, 2.25]$ that the first instability of the coupled system is well predicted by examining the stability of the sole wake. Clearly, the (χ, *Re*) and (*St*, *Re*) phase diagrams are much more complex for the

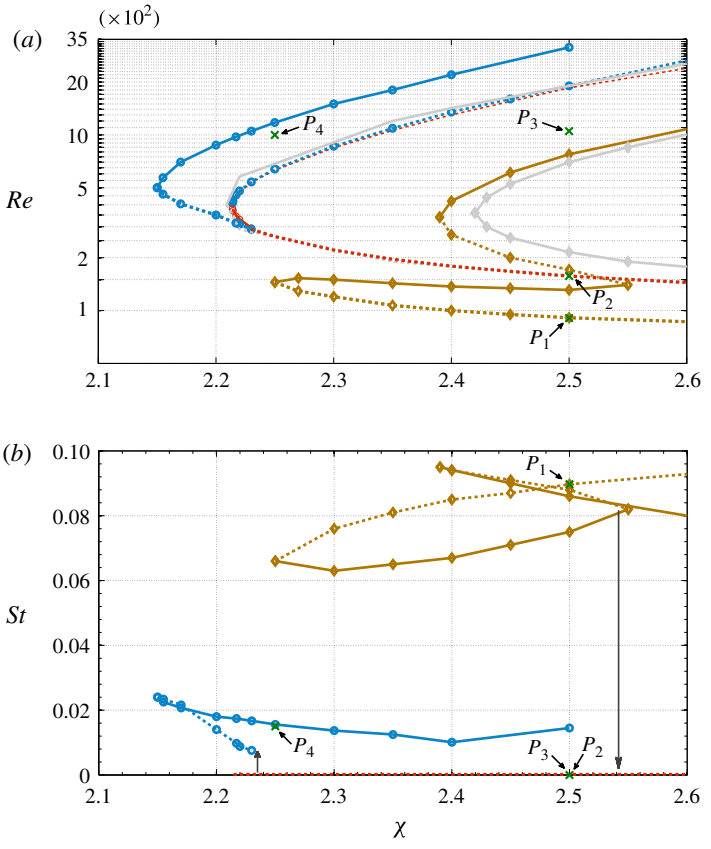

FIGURE 2. Phase diagram (χ, Re) showing the neutral stability curves for a freely rising and a fixed (grey) bubble. The thick dashed (solid) lines correspond to destabilization (restabilization) thresholds. Lines with diamonds (circles) correspond to high- (low-) frequency modes while the thick red dashed line without symbols corresponds to stationary modes. The thin red dashed line shows the location where the merges of (or splits into) stationary modes occur. The green crosses mark the locations of points P_1–P_4 discussed in § 3.3.

coupled system. In figure ⌜(*a*), the critical curve corresponding to the stationary mode and that corresponding to the *HF* (respectively *LF*) mode are observed to cross at $(\chi, Re) \simeq (2.53, 151)$ (respectively $\simeq (2.23, 290)$), yielding codimension-two points of steady-Hopf/*HF* and steady-Hopf/*LF* type, respectively. Moving along the marginal curve of the primary instability, these codimension-two points are loci where a sudden frequency jump identified by an arrow in figure ⌜(*b*) takes place.

3.3. *Global modes and comparison with DNS results*

Figure ⌜ displays the spatial structure of a few critical global modes corresponding to points P_1 to P_4 in figure ⌜(*a*), their magnitude being normalized in such a way that the bubble inclination is unity. The above points were selected to allow comparisons with the DNS results of MM02.

Figure ⌜(*a*,*b*) reveals the wake structure of the *LF* mode that takes place at P_4 ($\chi = 2.25$, $Re = 10^3$). The corresponding axial vorticity keeps a constant sign

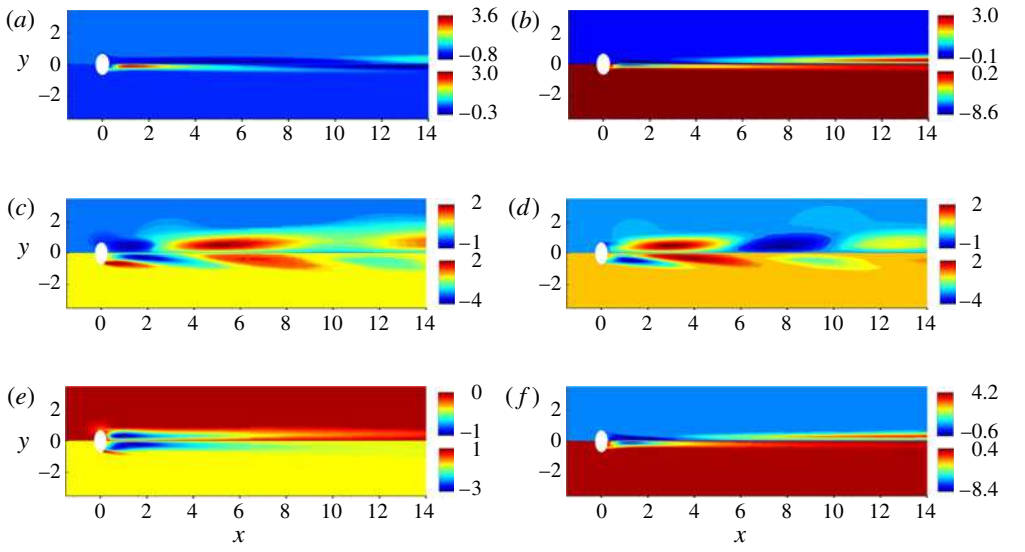

FIGURE 3. Several global modes ($m = 1$) of the coupled system at points P_1–P_4 in figure (a). The upper (lower) half of each subfigure displays the isovalues of the axial velocity (vorticity) of the mode; gravity acts from left to right. (*a*,*b*) The *LF* mode at P_4 ($\chi = 2.25$, $Re = 10^3$). (*c*,*d*) The *HF* mode at P_1 ($\chi = 2.5$, $Re = 90.6$) (in both cases, (*a*,*c*,*e*) and (*b*,*d*,*f*) display the real and imaginary parts, respectively). (*e*,*f*) The stationary modes at P_2 ($\chi = 2.5$, $Re = 157.3$) and P_3 ($\chi = 2.5$, $Re = 1050$), respectively; for these two modes, the axial velocity (vorticity) is purely real (imaginary).

over a long distance (typically ten bubble diameters), which makes the near wake look similar to that associated with a strictly stationary mode (compare with panels *e* and *f*). However, Tchoufag *et al.* ( ) showed that the real and imaginary parts of an unsteady mode actually correspond to two different instants of time in its dynamics. Hence, comparison of panels (*a*) and (*b*) proves that the axial velocity and vorticity disturbances change sign as time evolves, although over a long time period. Such dynamics are reminiscent of the DNS observations of MM02 and Mougin & Magnaudet ( ), who found that in the zigzagging (*ZZ*) regime, high-Reynolds-number bubbles are followed by a pair of counter-rotating trailing vortices that change sign every half-period of the zigzag (see also the experimental observations in ultrapure water reported by de Vries, Biesheuvel & van Wijngaarden , van Wijngaarden and Veldhuis, Biesheuvel & van Wijngaarden). To go beyond this qualitative resemblance, we may compare the frequency of the present mode with that found in the DNS run of MM02 corresponding to $\chi = 2.25, Ar = 390$. In this run, the straight vertical path eventually switches to a *ZZ* path (figure a). Starting from rest, the Reynolds number $Re(t)$ (based on the norm of $\boldsymbol{U}$) first increases rapidly until it reaches a maximum $Re(t) = Re_{max}$ close to but slightly less than that corresponding to the equilibrium value in the base state, $Re_0 \approx 1275$. Then, $Re(t)$ somewhat decreases when the instability develops (owing to the supplementary drag resulting from the occurrence of the trailing vortices) and eventually oscillates during the *ZZ* path. Since the bifurcation and the *ZZ* path both take place at an $O(10^3)$ Reynolds number, the comparison with the linear mode at P_4 is relevant. However, it must be kept in mind that this mode was obtained assuming a strictly steady axisymmetric base flow, whereas the flow in the DNS evolves in time at previous

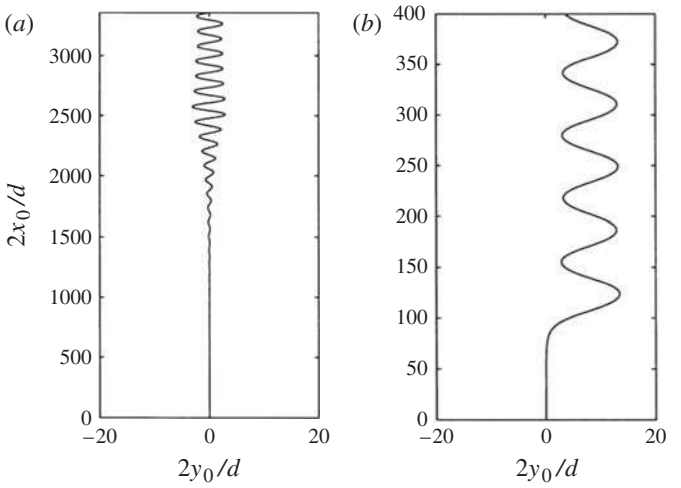

FIGURE 4. Path of two oblate bubbles corresponding to $Ar = 390$ with aspect ratio (*a*) $\chi = 2.25$ and (*b*) $\chi = 2.5$. In both cases, the whole system is initially at rest (reprinted from Mougin).

stages and is three-dimensional far before the conditions corresponding to P_4 are reached, since figure (*a*) indicates that the stationary mode becomes unstable at $Re \approx 270$ for this aspect ratio. Defining the reduced frequency normalized by the gravitational velocity, $\tilde{St} = St\, U_0/U_g$, we find it to be $\tilde{St} \simeq 0.042$ for the linear *LF* mode at its restabilization threshold ($Re \approx 1180$), which compares reasonably well with the DNS finding, $\tilde{St}_{DNS} \simeq 0.053$, corresponding to figure (*a*). This agreement, although not perfect for the reasons outlined above, supports the idea that, in this range of χ, the zigzagging motion of bubbles with $O(10^3)$ Reynolds numbers is associated with an *LF* mode, as figure (*a*) predicts.

Let now turn to the *HF* mode at an $O(10^2)$ Reynolds number shown in figure (*c*,*d*). Comparison of the two panels makes it clear that the spatial arrangement of the axial velocity evolves periodically from a 'sign-preserving' type (all 'rolls' in the wake keep the same sign) to a 'sign-alternating' type (two successive rolls have opposite signs), a switch that Tchoufag *et al.* ( ) showed to be indicative of a strong coupling between the body and its wake at the corresponding bifurcation. It is then no surprise that the fixed-bubble approach could not predict the bifurcation that takes place at P_1. As figure (*a*) indicates, point P_1 corresponds to the first bifurcation (with increasing *Re*) for the aspect ratio $\chi = 2.5$. This bifurcation is of Hopf type, and the threshold, once expressed using the gravitational velocity, is found to be $Ar \simeq 90.5$. These findings are in good agreement with those of MM02, whose DNS predicted the threshold of the zigzagging path to take place at $Ar_{DNS} \simeq 86$ when $\chi = 2.5$. Moreover, the frequency $\tilde{St}$ is approximately 0.095 for the *HF* mode, which also compares well with the DNS prediction $\tilde{St}_{DNS} \simeq 0.092$.

As shown in figure (*e*,*f*), the wake associated with the stationary modes at P_2 ($Re = 157.3$) and P_3 ($Re = 1050$), both for $\chi = 2.5$, is dominated by the presence of two counter-rotating trailing vortices, a wake structure known to result in a steady non-zero lift force. At P_2, the near wake also involves two small secondary vortices of opposite sign directly connected to the bubble, a feature that does not exist at P_3. This difference may be understood by noting that, unlike the case of solid bodies,

the standing eddy at the rear of a bubble shrinks as Re becomes very large (Blanco & Magnaudet ; Magnaudet & Mougin), so that the streamline distribution in the base flow gets closer to that corresponding to the potential flow past an oblate spheroid. This change is also responsible for the narrowing of the wake as Re increases, which tends to 'glue' the trailing vortices to the symmetry axis, as figure (*f*) reveals. Again, a comparison with the DNS predictions can be achieved in the latter case. With $\chi = 2.5$ and $Ar = 390$, MM02 found the bubble Reynolds number to reach a maximum $Re_{max} \approx 1035$ before the path departed from vertical. Then, this path was observed to experience a marked lateral drift until a periodic ZZ motion eventually set in (see figure *b*). As the Reynolds number at P_3 is close to Re_{max}, it is again reasonable to consider that the linear mode at P_3 represents a good approximation of the mode that first becomes unstable in the DNS. Since we found the former to be stationary, LSA allows us to conclude that the first bifurcation experienced by the system when $Re(t)$ becomes of $O(Re_{max})$ yields a steady oblique (SO) path, a prediction in agreement with figure (*b*).

4. Summary and final comments

In this work, we investigated the global linear stability of the path of an oblate spheroidal bubble rising in a Newtonian fluid otherwise at rest. The computed eigenvalues and modes of the coupled fluid + bubble system revealed a much more complex behaviour than in the case where the stability of the sole wake is considered. In particular, we found that the first instability of the system as the Reynolds number increases may arise through a Hopf bifurcation associated with a low- or high-frequency mode, depending on the aspect ratio, while it always occurs through a stationary bifurcation when the bubble is set fixed. Comparisons with DNS results performed for several sets of χ and Ar showed that the nature and frequency (if any) of the mode that first becomes unstable are well captured by the present LSA approach. However, several open issues remain.

First, as we have already mentioned, comparison of LSA results with experimental and DNS observations is not straightforward because bubbles observed in 'real life' are generally released from rest, which makes their rise Reynolds number highly time-dependent, especially during the initial transient. This raises a question about the type of instability that actually develops when the aspect ratio is such that the physical system successively explores several unstable regions as $Re(t)$ evolves. This is, for instance, the case for the bubble with $\chi = 2.25$, $Ar = 390$ we discussed in the previous section, which according to figure (*a*) crosses the region where the S mode is unstable when it accelerates and its Reynolds number is in the range $270 \lesssim Re(t) \lesssim 630$, before it enters the region where the LF mode is unstable when it gets closer to its steady state. In that case, the comparison we performed with DNS data revealed that the final non-vertical path exhibits characteristics consistent with those of the linear LF mode; the only discernible trace of the S mode is probably the slight difference we observed in the values of $\tilde{St}$, which may presumably be attributed to the three-dimensionality of the flow that has already set in before the LF mode becomes unstable. However, the influence of modes that are unstable during some stage of the initial transient is probably more severe in certain cases, such as for instance with bubbles such that $2.3 \lesssim \chi \lesssim 2.35$ and Ar values yielding final Reynolds numbers slightly beyond the destabilization threshold of the LF mode (the dotted line with blue open circles in figure *a*). Here, the system successively covers ranges of $Re(t)$ where the HF, S and LF modes are unstable. In particular, it spends

a significant amount of time in the intermediate region where the stationary mode is unstable. Since the growth rate of this mode is much larger than that of the other two according to figure (*a*), one may guess that the late evolution of the real system carries some footprint of this *S* mode. Unfortunately, MM02 did not perform any run with such (χ, Ar) sets and we cannot check this conjecture here.

A similar difficulty is encountered after the bubble has reached its maximum Reynolds number and may be illustrated with the example of figure (*b*). Here, $Re(t)$ reaches its maximum value, $Re_{max} \simeq 1035$, before the *SO* path sets in. During this second stage, $Re(t)$ sharply decreases due on the one hand to the supplementary drag induced by the trailing vortices and on the other hand to the inclination of the path which lowers the driving component of the buoyancy force. At the end of the *SO* stage, $Re(t)$ is approximately 800 which, according to figure (*a*), is close to the upper threshold of the *HF* mode. Therefore, looking at the path displayed in figure (*b*), it is tempting to conclude that the *ZZ* stage that succeeds the oblique drift corresponds to this *HF* mode. Actually this is not so, since the frequency of the latter yields $\tilde{St} \simeq 0.175$ according to figure (*b*), while the frequency determined in the DNS is $\tilde{St}_{DNS} \simeq 0.064$. A weakly nonlinear approach is required to address the above issues and determine how the primary modes that are successively encountered as $Re(t)$ evolves interact and what the essential characteristics of the final stage of the system are. We are currently developing such an approach.

Comparison of the present predictions with known results for real bubbles raises another issue. According to the experimental findings of Zenit & Magnaudet ( ) obtained with various silicone oils, the path may become unstable for aspect ratios typically 10 % smaller than the critical value predicted here. Moreover, for $O(10^2)$ Reynolds numbers, Zenit & Magnaudet ( ) showed that the wake structure is very similar to that corresponding to the *LF* mode displayed in figure (*a*,*b*) (with, in addition, the pair of secondary vortices found in the same range of *Re* in the *S* mode of figure (*c*). We would guess that both features result from the slight fore–aft asymmetry of real nearly spheroidal bubbles: not only might this asymmetry shift the marginal curve toward smaller χ, as suggested by the numerical study of Cano-Lozano, Bohorquez & Martinez-Bazan ( ), but it also seems to deform the stability diagram in such a way that the threshold corresponding to the destabilization of the *LF* mode is shifted toward much smaller Reynolds numbers than for perfectly spheroidal bubbles and may, over a significant range of χ, be the first that becomes unstable as *Re* increases. We are currently working on this aspect by introducing more realistic bubble shapes in our LSA code.

Finally, the existence of a crescent-shaped region in figure (*a*) within which the *S* mode is unstable provided the aspect ratio is larger than 2.215 raises an interesting puzzle. Indeed, this prediction suggests that bubbles whose final Reynolds number falls in this region should eventually follow an *SO* path. This is especially clear within the narrow range $2.23 \leqslant \chi \leqslant 2.25$ where the *S* mode is associated with the primary bifurcation, i.e. no previous bifurcation can alter the final behaviour of the system. The point is that we are not aware of any experimental or computational observation that supports the existence of such an inclined path, except during short transients as in figure (*b*) (again MM02 did not consider any (χ, Ar) set whose final state should have fallen in this region). Only zigzagging or spiralling paths have been observed to subsist over long periods of time, suggesting that the *SO* path is not a solution of the full nonlinear problem. This is at odds with the case of solid spheres and disks for which such a path has been consistently reported, in both experiments and computations, and was predicted to be a stable non-trivial solution

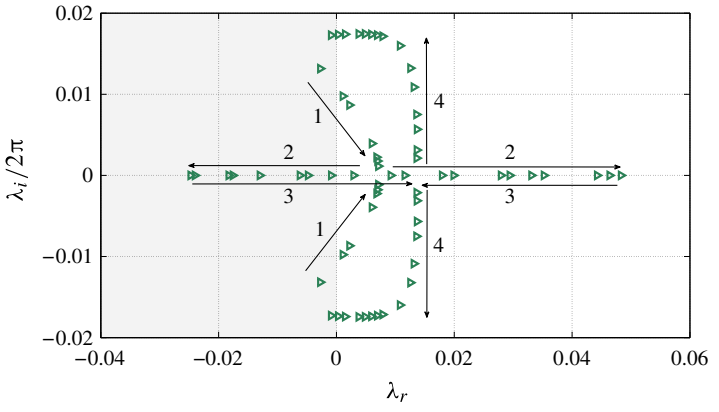

FIGURE 5. Complex path of the unstable eigenvalue found with a bubble of aspect ratio $\chi = 2.217$. The left grey part of the plane indicates the region where the corresponding eigenmode is stable.

of the fluid + body problem though a weakly nonlinear analysis by Fabre, Tchoufag & Magnaudet ( ). Crucial in this analysis is the fact that the torque experienced by the body vanishes for a small non-zero inclination of the path. It might be that the shear-free rather than no-slip condition that holds at a bubble surface changes the nature of the bifurcation that yields the *SO* path: it was found to be supercritical for spheres and disks (except when the latter are extremely thin) and could be subcritical for bubbles. We are currently repeating the analysis developed by Fabre *et al.* ( ) with a bubble to check this possibility.

Acknowledgement

This work was supported by the Agence Nationale de la Recherche under grant ANR-09-BLAN-0132 OBLIC.

Appendix. Merging/splitting of eigenvalues in the complex plane

To facilitate the understanding of the merging/splitting behaviour exhibited by several eigenvalues in figure , figure shows how the eigenvalue with the largest real part found for $\chi = 2.217$ evolves in the complex plane. We selected this example as a prototype of eigenvalues whose imaginary part vanishes in some range of Re, then yielding a stationary mode. The arrows in figure indicate the direction of increasing Re, from 1 to 4. Following arrows 1, we first observe a pair of complex conjugate eigenvalues with a negative real part. This real part then changes sign, leading to an instability corresponding to an *LF* mode, until the two eigenvalues merge at point $(0.007, 0)$. There they give birth to a pair of real eigenvalues. Following the arrow 2 pointing to the right, one of them (which corresponds to the main stationary mode in figure) is seen to increase until it reaches the point $(0.048, 0)$. The second real eigenvalue (corresponding to the subdominant stationary mode in figure) decreases along the second arrow 2 and changes sign (i.e. the corresponding mode restabilizes) until it reaches the point $(-0.025, 0)$. Then, following arrows 3, these two eigenvalues go through their previous paths in the reverse direction. They eventually merge at point $(0.014, 0)$ where they split into a new pair of complex conjugate eigenvalues

(corresponding to a second *LF* mode). Following arrows 4, the magnitude of their imaginary part sharply increases without much change in the real part, until it saturates at a value of ± 0.017. Then, the real part sharply decreases and eventually becomes negative, leading to restabilization.

References

ASSEMAT, P., FABRE, D. & MAGNAUDET, J. 2012 The onset of unsteadiness of two-dimensional bodies falling or rising freely in a viscous fluid: a linear study. *J. Fluid Mech.* **690**, 173–202.

AUGUSTE, F., MAGNAUDET, J. & FABRE, D. 2013 Falling styles of disks. *J. Fluid Mech.* **719**, 388–405.

BLANCO, A. & MAGNAUDET, J. 1995 The structure of the axisymmetric high-Reynolds number flow around an ellipsoidal bubble of fixed shape. *Phys. Fluids* **7**, 1265–1274.

CANO-LOZANO, J. C., BOHORQUEZ, P. & MARTINEZ-BAZAN, C. 2013 Wake instability of a fixed axisymmetric bubble of realistic shape. *Intl J. Multiphase Flow* **51**, 11–21.

CHRUST, M., BOUCHET, G. & DUSEK, J. 2013 Numerical simulation of the dynamics of freely falling discs. *Phys. Fluids* **25**, 044102.

CHRUST, M., BOUCHET, G. & DUSEK, J. 2014 Effect of solid body degrees of freedom on the path instabilities of freely falling or rising flat cylinders. *J. Fluids Struct.* **47**, 55–70.

ELLINGSEN, K. & RISSO, F. 2001 On the rise of an ellipsoidal bubble in water: oscillatory paths and liquid-induced velocity. *J. Fluid Mech.* **440**, 235–268.

FABRE, D., TCHOUFAG, J. & MAGNAUDET, J. 2012 The steady oblique path of buoyancy-driven disks and spheres. *J. Fluid Mech.* **707**, 24–36.

MAGNAUDET, J. & EAMES, I. 2000 The motion of high-Reynolds-number bubbles in inhomogeneous flows. *Annu. Rev. Fluid Mech.* **32**, 659–708.

MAGNAUDET, J. & MOUGIN, G. 2007 Wake instability of a fixed spheroidal bubble. *J. Fluid Mech.* **572**, 311–337.

MOUGIN, G. 2002 Interactions entre la dynamique d'une bulle et les instabilités de son sillage. PhD thesis, Inst. Nat. Polytech. Toulouse, France.

MOUGIN, G. & MAGNAUDET, J. 2002 Path instability of a rising bubble. *Phys. Rev. Lett.* **88**, 014502.

MOUGIN, G. & MAGNAUDET, J. 2006 Wake-induced forces and torques on a zigzagging/spiralling bubble. *J. Fluid Mech.* **567**, 185–194.

NATARAJAN, R. & ACRIVOS, A. 1993 The instability of the steady flow past spheres and disks. *J. Fluid Mech.* **254**, 323–344.

PROSPERETTI, A. 2004 Bubbles. *Phys. Fluids* **16**, 1852–1865.

PROSPERETTI, A., OHL, C., TIJINK, A., MOUGIN, G. & MAGNAUDET, J. 2003 Leonardo's paradox (Appendix to 'The added mass of an expanding bubble' by C. D. Ohl, A. Tijink and A. Prosperetti). *J. Fluid Mech.* **482**, 271–290.

SIPP, D. & LEBEDEV, A. 2007 Global stability of base and mean-flows: a general approach and its applications to cylinder and open cavity flows. *J. Fluid Mech.* **593**, 333–358.

TCHOUFAG, J., FABRE, D. & MAGNAUDET, J. 2014 Global linear stability analysis of the wake and path of buoyancy-driven disks and thin cylinders. *J. Fluid Mech.* **740**, 278–311.

TCHOUFAG, J., MAGNAUDET, J. & FABRE, D. 2013 Linear stability and sensitivity of the flow past a fixed oblate spheroidal bubble. *Phys. Fluids* **25**, 054108.

VELDHUIS, C., BIESHEUVEL, A. & VAN WIJNGAARDEN, L. 2008 Shape oscillations on bubbles rising in clean and in tap water. *Phys. Fluids* **20**, 040705.

DE VRIES, A., BIESHEUVEL, A. & VAN WIJNGAARDEN, L. 2002 Notes on the path and wake of a gas bubble rising in pure water. *Intl J. Multiphase Flow* **28**, 1823–1835.

VAN WIJNGAARDEN, L. 2005 Bubble velocities induced by trailing vortices behind neighbours. *J. Fluid Mech.* **541**, 203–229.

ZENIT, R. & MAGNAUDET, J. 2008 Path instability of rising spheroidal air bubbles: a shape-controlled process. *Phys. Fluids* **20**, 061702.

ZENIT, R. & MAGNAUDET, J. 2009 Measurements of the streamwise vorticity in the wake of an oscillating bubble. *Intl J. Multiphase Flow* **35**, 195–203.